Development of an Air-Bearing-Based Satellite Attitude Simulator and Testing of an ADCS Solution

Bruno Alexandre Morais Dias Ribeiro
bruno.d.ribeiro@tecnico.ulisboa.pt

Instituto Superior Técnico, Universidade de Lisboa, Portugal

March 2021

Abstract

There is a recent growth on the interest for nanosatellite technology. A key particularity of space projects is the difficulty to test the technologies in a realistic environment before the mission is deployed. The main goal of this work is to help the NANOSTAR project to overcome this difficulty by designing a prototype to test the ADCS and provide grounded studies on the attitude control and determination algorithms that can be employed in the missions. To this end, a low-cost ADCS is designed, having momentum wheels and magnetorquers as actuators. Attitude estimation is based on vector measurements provided by a magnetometer, rate gyroscope and accelerometer. Two optimal control strategies are used for Nadir pointing using the momentum wheels, namely, an LQR controller and an LQR controller with integral action. Detumbling and momentum dumping are accomplished through the use of magnetorquers. Three estimation filters are considered, two based on Kalman filtering, one of them formulated on Euler angles and the other on quaternion. The third filter is based on the SLERP technique. The control and estimation algorithms are tested in a software simulator that describes the space environment realistically. Then, a test bench and a CubeSat prototype are designed and built, allowing to test the algorithms on ground. Results for the ADCS system performance are presented both from the simulation and the experimental environments.
Keywords: Nanosatellites, Optimal Control, Complementary Filters, Ground-testing

1. Introduction

A particularly relevant type of small satellite is the CubeSat, developed by California Polytechnic State University and Stanford University in 1999 with educational purposes [5]. The ADCS is a critical subsystem in a nanosatellite [2]. In fact, only 20% of pico and nanosatellites are left tumbling free in space and about 15% of pico and nanosatellites are equipped with control to point an instrument.

To test the technologies before the mission is deployed, ADCS are tested in a computer simulation against realistic models of the conditions it will be subject to in orbit. Nevertheless, ADCS development and hardware in the loop verification of momentum exchange devices can largely benefit from ground testing [8]. Since the beginning of the space race, air bearing based platforms have been used for simulating the torque-free conditions in space.

Attitude determination of a spacecraft means determining its orientation in space with respect to a given reference frame. There are static and recursive methods. The first are memory-less, meaning that each time the attitude is determined is independent from the others. The most used static methods are, by chronological order [7]: the TRIAD algorithm; Davenport's solution to the Wahba's problem; the QUEST algorithm. Recursive methods take advantage from past measurements to provide more accurate solutions. The most popular recursive algorithm is the Kalman Filter [6].

Spacecraft attitude stabilization methods can be divided into two types. Passive techniques such as Gravity Gradient stabilization, Passive Magnetic Stabilization, and Aerodynamic stabilization in Low Earth Orbit take advantage of the geometric and magnetic design of a satellite and the orbit properties to passively provide attitude stabilization and rough pointing. More capable on-board computers allow for more demanding pointing requirements, by means of active control, namely three-axis stabilization. For CubeSats, magnetorquers [16] are often the primary actuator for attitude control due to their simplicity and low cost. Designs adopting reaction / momentum wheels as primary actuators and magnetotorquers for momentum dumping provide better pointing accuracy.

Air bearing based platforms can be divided into 3 types. Planar platforms provide two translational

degrees of freedom and oftentimes also one rotational (vertical spin) [12]. These platforms provide almost frictionless planar sliding motion on a flat surface. Vertical spin motion can be added using a reaction wheel or compressed air thrusters. Rotational systems, aim at providing a frictionless rotational movement with three degrees of freedom. Depending on the geometry of the platform, the pitch, yaw or roll rotations may be limited. *Tabletop* and *Umbrella* systems guarantee full freedom yaw rotation and limited pitch and roll rotations. *Dumbbell* systems guarantee full freedom yaw and roll rotations and limited pitch rotation. The last type are combinational systems that often provide 5 to 6 DOF. The testbed presented in this work is a rotational system, even though it does not fit in any of the 3 presented categories.

Although primarily designed for educational purposes, the proposed testbed application reaches beyond it to any payload onboard a nanosatellite requiring attitude control. The testbed allows any ADCS containable withing the 1U standard to go through testing prior to launch.

2. Background

2.1. Reference Frames

The Body-Fixed frame is centered at the center of mass of the spacecraft. The $\mathbf{Z}_b$ axis is aligned with the main scientific payload. The $\mathbf{X}_b$ axis is aligned with the normal to the bottom plate of the spacecraft. The $\mathbf{Y}_b$ axis follows the right hand rule.

The origin of the Earth-Centered Inerital (ECI) frame is the center of the Earth. The $\mathbf{X}_I$ is the direction from the Earth center to the vernal equinox. The $\mathbf{Z}_I$ axis is the Earth rotational axis. The $\mathbf{Y}_I$ follows the right-hand rule.

The origin of the Local Vertical Local Horizontal (LVLH) frame is the center of mass of the spacecraft. The $\mathbf{X}_{lvlh}$ direction is the same as the spacecraft velocity. The $\mathbf{Z}_{lvlh}$ is Nadir pointing. The $\mathbf{Y}_{lvlh}$ follows the right-hand rule.

2.2. Attitude Kinematics and Dynamics

In the present work, the unit quaternion is used to represent the rotation from the ECI or LVLH to the Body frame. Denoting the quaternion by $\bar{\mathbf{q}}$ and the angular velocity of the Body frame relative to the reference frame by $\mathbf{w}$, the kinematics is [16]:

$$\frac{d\bar{\mathbf{q}}}{dt} = \bar{\mathbf{q}}(t) \otimes (0 + \frac{1}{2}\mathbf{w}(t)). \tag{1}$$

For a Nadir Pointing spacecraft, the attitude of the spacecraft is represented by the rotation of the spacecraft body frame relative to the LVLH frame. The quaternion and body rate are measured with respect to the LVLH frame. Denoting the angular momentum of the momentum wheels system in the body frame by $\mathbf{h}_w = [h_1, h_2, h_3]^T$, the LVLH frame rate with respect to the inertial frame represented in the Body frame by $\mathbf{w}^b_{lvlh}$, the body rate with respect to the LVLH frame represented in the body frame by $\mathbf{w}$, the control torque by $\mathbf{u}$ and the torque perturbation by $\mathbf{t}_d$, the Nadir Pointing Momentum Biased Spacecraft dynamics can be expressed by the following equation [16]:

$$\mathbf{J}\dot{\mathbf{w}} = \mathbf{f}(\mathbf{w}, \mathbf{w}^b_{lvlh}, \mathbf{h}_w) + \mathbf{t}_d + \mathbf{u}. \tag{2}$$

$$\begin{aligned}\mathbf{f}(\mathbf{w}, \mathbf{w}^b_{lvlh}, \mathbf{h}_w) =& \mathbf{J}(\mathbf{w} \times \mathbf{w}^b_{lvlh}) - \mathbf{w} \times (\mathbf{J}\mathbf{w}) \\ &- \mathbf{w} \times (\mathbf{J}\mathbf{w}^b_{lvlh}) - \mathbf{w}^b_{lvlh} \times (\mathbf{J}\mathbf{w}) \\ &- \mathbf{w}^b_{lvlh} \times (\mathbf{J}\mathbf{w}^b_{lvlh}) - \mathbf{w} \times \mathbf{h}_w \\ &- \mathbf{w}^b_{lvlh} \times \mathbf{h}_w.\end{aligned}$$

For small angles, the gravity gradient torque can be approximated as in [13] so that linearization around the nominal momentum wheel system angular momentum $\mathbf{h}^n_w = [h^n_1, h^n_2, h^n_3]^T$, zero body rate $\mathbf{w} = [0, 0, 0]^T$ and $\bar{\mathbf{q}} = [1, 0, 0, 0]^T$, yields

$$\begin{bmatrix}\dot{\mathbf{w}} \\ \dot{\mathbf{q}}\end{bmatrix} = \begin{bmatrix}\mathbf{J}^{-1}\mathbf{A}_1 & \mathbf{J}^{-1}\mathbf{A}_2 \\ \frac{1}{2}\mathbf{I}_3 & \mathbf{0}_3\end{bmatrix}\begin{bmatrix}\mathbf{w} \\ \mathbf{q}\end{bmatrix} + \begin{bmatrix}\mathbf{J}^{-1} \\ \mathbf{0}_3\end{bmatrix}\mathbf{u}, \tag{3}$$

where $\mathbf{A}_1$ and $\mathbf{A}_1$ are given by

$$\mathbf{A}_1 = \begin{bmatrix}0 & -h^n_3 & a_1 + h^n_2 \\ h^n_3 & 0 & -h^n_1 \\ -a_1 - h^n_2 & h^n_1 & 0\end{bmatrix}, \tag{4}$$

$$\mathbf{A}_2 = \begin{bmatrix}a_2 + 2h^n_2 w_0 & 0 & 0 \\ -2h^n_1 w_0 & a_3 & -2h^n_3 w_0 \\ 0 & 0 & a_4 + 2h^n_2 w_0\end{bmatrix}, \tag{5}$$

where $a_1 = (J_{11} - J_{22} + J_{33})w_0$, $a_2 = 8w_0^2(J_{33} - J_{22})$, $a_3 = 6w_0^2(J_{33} - J_{11})$, $a_4 = 2w_0^2(J_{11} - J_{22})$.

3. Attitude Control

3.1. Nominal Mode

The nominal model corresponds to Nadir Pointing, i.e. aligning the Body and LVLH frames. For the previously described Nadir pointing momentum biased spacecraft model, this corresponds to regulating the state $[\mathbf{w}, \mathbf{q}]$. A Linear Quadratic Regulator with Integral Action solution will be studied and compared against the LQR without Integral Action. Consider the discrete-time LTI system:

$$\begin{aligned}\mathbf{x}_{k+1} &= \mathbf{A}\mathbf{x}_k + \mathbf{B}\mathbf{u}_k \\ \mathbf{y}_k &= \mathbf{C}x_k,\end{aligned} \tag{6}$$

where the subscript k identifies the sample at time kT, where T is the sampling period and k is an integer number. The state is $\mathbf{x}_k = [\mathbf{w}_k, \mathbf{q}_k]^T$ and the matrices $\mathbf{A}$ and $\mathbf{B}$ are obtained applying the forward Euler method to equation 3

$$\begin{bmatrix}\mathbf{w}_{k+1}\\ \mathbf{q}_{k+1}\end{bmatrix} = \begin{bmatrix}\mathbf{I}_3 + T\mathbf{J}^{-1}\mathbf{A}_1 & T\mathbf{J}^{-1}\mathbf{A}_2\\ \frac{T}{2}\mathbf{I}_3 & \mathbf{I}_3\end{bmatrix}\begin{bmatrix}\mathbf{w}_k\\ \mathbf{q}_k\end{bmatrix} + \begin{bmatrix}T\mathbf{J}^{-1}\\ \mathbf{0}_3\end{bmatrix}\mathbf{u}_k. \tag{7}$$

A thorough description of the LQR problem can be found on [3]. The minimization of the LQR performance index leads to the linear state feedback

$$\mathbf{u}_k = -\mathbf{K}_L\mathbf{x}_k. \tag{8}$$

The gain $\mathbf{K}_L$ can be obtained by the command *dlqr* from *MATLAB*.

A steady-state error may arise from unmodeled dynamics or disturbances. This drawback can be overcome by augmenting the state space with the integral of the attitude $\mathbf{q}$. The concept of integral feedback is described in detail in [15]. The regulation error can be defined as $\mathbf{z}_k = \mathbf{r} - \mathbf{C}\mathbf{x}_k$, where $\mathbf{r}$ is a constant reference. The reformulated dynamic model is given by

$$\begin{bmatrix}\mathbf{z}_{k+1}\\ \Delta\mathbf{x}_{k+1}\end{bmatrix} = \begin{bmatrix}\mathbf{I} & -\mathbf{C}\mathbf{A}\\ \mathbf{0} & \mathbf{A}\end{bmatrix}\begin{bmatrix}\mathbf{z}_k\\ \Delta\mathbf{x}_k\end{bmatrix} + \begin{bmatrix}-\mathbf{C}\mathbf{B}\\ \mathbf{B}\end{bmatrix}\Delta\mathbf{u}_k, \tag{9}$$

where $\Delta\mathbf{u}_k = \mathbf{u}_k - \mathbf{u}_{k-1}$ and $\Delta\mathbf{x}_k = \mathbf{x}_k - \mathbf{x}_{k-1}$. The sampling time is omitted for simplicity, meaning that kT is replaced by k. Applying the regulator problem, the constant gain $\mathbf{K}_L = [\mathbf{K}_z, \mathbf{K}_x]$ is obtained.

3.2. Momentum Dumping

Magnetic torquers are commonly used in low-Earth orbiting spacecraft for momentum dumping. The torque generated by magnetic torquers is given by

$$\mathbf{T} = \mathbf{m} \times \mathbf{B}_m, \tag{10}$$

where $\mathbf{m}$ $[Am^2]$ is the commanded magnetic dipole moment generated by the torquers and $\mathbf{B}_m$ [T] is the local geomagnetic field expressed in body-frame coordinates. A common approach to design a magnetorquer control law for momentum dumping is to command a magnetic dipole moment [7]:

$$\mathbf{m} = \frac{k_{md}}{|\mathbf{B}_m|}\Delta\mathbf{h}_w \times \mathbf{b}, \tag{11}$$

where $\Delta\mathbf{h}_w$ is the momentum wheel system angular momentum tracking error, $\mathbf{b} = \mathbf{B}_m/|\mathbf{B}_m|$ and k_{md} is a positive scalar gain. Let's denote the resulting torque by $\mathbf{T}_{md}$. The use of this torque in addition to the LQR feedback, $\mathbf{T}_c$, results in an excess of torque in the spacecraft. To counteract this, a despin torque is imposed on each wheel:$\mathbf{T}_{wmd} = \mathbf{T}_{md}$.

3.3. Detumbling Mode

The proposed controller for detumbling consists on commanding the following magnetic dipole moment:

$$\mathbf{m} = \frac{k_{det}}{|\mathbf{B}_m|}\mathbf{w}_I \times \mathbf{b}, \tag{12}$$

where $\mathbf{w}_I$ is the spacecraft's angular rate relative to the ECI frame, $\mathbf{b} = \mathbf{B}_m/|\mathbf{B}_m|$ and k_{det} is a positive scalar gain. The theory behind this control law can be found on [1]. In [7], stability of the present control law is proven if $\mathbf{J}$ is diagonal, resorting to Lyapunov Stability theory. Asymptotic stability is not guaranteed. According to [1], this is not a concern in practice, though. Reference [1] provides an expression for k_{det} based on analyzing the closed-loop dynamics of the component of $\mathbf{w}_I$ perpendicular to $\mathbf{B}_m$:

$$k_{det} = \frac{4\pi}{p}(1 + sin(i_m))J_{min}, \tag{13}$$

where p is the orbit period, i_m is its inclination and J_{min} is the minimum principal moment of inertia.

4. Attitude Determination

4.1. Euler-Based Complementary Filter

The description of the filter presented in this section is based on the work of [4].

Let $\boldsymbol{\lambda} = [\phi \quad \theta \quad \psi]^T$ be the vector containing the Euler angles roll, pitch and yaw respectively. The kinematics is given by $\dot{\boldsymbol{\lambda}} = \mathbf{Q}(\boldsymbol{\lambda})\boldsymbol{w}$, where $\boldsymbol{w} = [w_x w_y w_z]^T$ and

$$\mathbf{Q}(\boldsymbol{\lambda}) = \begin{bmatrix}1 & sin(\phi)tan(\theta) & cos(\phi)tan(\theta)\\ 0 & cos(\phi) & -sin(\phi)\\ 0 & sin(\phi)sec(\theta) & cos(\phi)sec(\theta)\end{bmatrix}. \tag{14}$$

The discrete-time equivalent is obtained applying the Euler method (also called forward Euler method):

$$\boldsymbol{\lambda}_{k+1} = \boldsymbol{\lambda}_k + \Delta t\mathbf{Q}(\boldsymbol{\lambda}_k)\boldsymbol{w}_k. \tag{15}$$

The observer proposed in [4] is

$$\begin{aligned}\begin{bmatrix}\hat{\boldsymbol{\lambda}}\\ \hat{\boldsymbol{b}}_{\boldsymbol{w1}}\\ \hat{\boldsymbol{b}}_{\boldsymbol{w2}}\end{bmatrix}_{k+1} &= \begin{bmatrix}\mathbf{I} & -\Delta t\mathbf{Q}(\boldsymbol{\lambda}_k) & -\Delta t\mathbf{Q}(\boldsymbol{\lambda}_k)\\ \mathbf{0} & \mathbf{I} - \Delta t\mathbf{T}^{-1} & \mathbf{0}\\ \mathbf{0} & \mathbf{0} & \mathbf{I}\end{bmatrix}\begin{bmatrix}\hat{\boldsymbol{\lambda}}\\ \hat{\boldsymbol{b}}_{\boldsymbol{w1}}\\ \hat{\boldsymbol{b}}_{\boldsymbol{w2}}\end{bmatrix}_k\\ &\quad + \begin{bmatrix}\Delta t\mathbf{Q}(\boldsymbol{\lambda}_k)\\ \mathbf{0}\\ \mathbf{0}\end{bmatrix}\boldsymbol{w}_{sk},\\ &\quad + \begin{bmatrix}\mathbf{Q}(\boldsymbol{\lambda}_k)(\boldsymbol{K}_{\boldsymbol{1\lambda}} - \mathbf{I}) + \mathbf{Q}(\boldsymbol{\lambda}_{k-1})\\ \boldsymbol{K}_{\boldsymbol{2\lambda}}\\ \boldsymbol{K}_{\boldsymbol{3\lambda}}\end{bmatrix}(\boldsymbol{y}_{\boldsymbol{\lambda k}} - \hat{\boldsymbol{y}}_{\boldsymbol{\lambda k}})\end{aligned} \tag{16}$$

where $\hat{\mathbf{y}}_{\lambda_k} = \mathbf{Q}^{-1}(\lambda_{k-1})\hat{\boldsymbol{\lambda}}_k$, $\mathbf{y}_{\lambda k} = \mathbf{Q}^{-1}(\lambda_{k-1})\boldsymbol{\lambda}_k + \boldsymbol{\Theta}_k$ and $\boldsymbol{y}_{\lambda k}$ is the measured Euler angles transformed to the space of the angular rate and corrupted by zero-mean white Gaussian-noise $\boldsymbol{\Theta}$. The attitude observation $\hat{\boldsymbol{\lambda}}$ can be obtained by measuring the Earth's gravitational and magnetic fields by an IMU. The observer gains are equal to the Kalman gain, $\mathbf{K} = [\mathbf{K}_{1\lambda}, \mathbf{K}_{2\lambda}, \mathbf{K}_{3\lambda}]^T$, from the auxiliary LTI system presented in [4], where the asymptotic stability of the observer 16 is proved if the pitch is bounded $|\theta| < \theta_{max} < \frac{\pi}{2}$.

4.2. Quaternion-Based Complementary Filter

This filter was inspired by the work of [10]. Firstly, the quaternion from Earth's gravity and magnetic fields observations is computed.

In the prediction step, the angular velocity vector from the rate gyros is used to compute an estimation of the orientation in quaternion form by applying the Euler method to equation 1.

In the update step, the SLERP technique (see [14]) is used to find an intermediate quaternion between the one from the prediction step and the one that comes from the Earth's gravity and magnetic fields observations.

4.3. Quaternion-Based Kalman Filter

The kinematics of the quaternion is given by equation 1 that can be rewritten, for simplification, as $\dot{\boldsymbol{q}} = \mathbf{F}(\mathbf{q})\mathbf{w}$. The discrete-time equivalent is:

$$\mathbf{q}_{k+1} = \mathbf{q}_k + \Delta t \mathbf{F}(\mathbf{q})\mathbf{w}. \tag{17}$$

The rate gyro measurement, is modeled as being affected by noise and rate random-walk (RRW). Incorporating the quaternion kinematics and the gyro noise model into a state-space model:

$$\begin{bmatrix}\mathbf{q}_{k+1}\\ \mathbf{b}_{k+1}\end{bmatrix} = \begin{bmatrix}\mathbf{I} & -\Delta t\mathbf{F}(\mathbf{q})\\ \mathbf{0} & \mathbf{I}\end{bmatrix}\begin{bmatrix}\mathbf{q}_k\\ \mathbf{b}_k\end{bmatrix} + \begin{bmatrix}\Delta t\mathbf{F}(\mathbf{q})\\ \mathbf{0}\end{bmatrix}\mathbf{w}rk + \begin{bmatrix}-\Delta t\mathbf{F}(\mathbf{q}) & \mathbf{0}\\ \mathbf{0} & \mathbf{I}\end{bmatrix}\begin{bmatrix}\mathbf{w}_{w_r k}\\ \mathbf{w}_{bk}\end{bmatrix}, \tag{18}$$

where $\mathbf{w}_{w_r}$ is zero-mean white Gaussian-noise; $\mathbf{b}_w$ is the gyro bias; $\mathbf{w}_b$ is the white Gaussian noise that affects the sensor bias. Linearizing the model 18 around $\bar{\mathbf{q}} = [1,0,0,0]^T$ and $\omega = [0,0,0]^T$ yields

$$\begin{bmatrix}\mathbf{q}_{k+1}\\ \mathbf{b}_{k+1}\end{bmatrix} = \begin{bmatrix}\mathbf{I} & -\frac{\Delta t}{2}\mathbf{I}\\ \mathbf{0} & \mathbf{I}\end{bmatrix}\begin{bmatrix}\mathbf{q}_k\\ \mathbf{b}_k\end{bmatrix} + \begin{bmatrix}\frac{\Delta t}{2}\mathbf{I}\\ \mathbf{0}\end{bmatrix}\mathbf{w}_{rk} + \begin{bmatrix}-\frac{\Delta t}{2}\mathbf{I} & \mathbf{0}\\ \mathbf{0} & \mathbf{I}\end{bmatrix}\begin{bmatrix}\mathbf{w}_{w_r k}\\ \mathbf{w}_{bk}\end{bmatrix}. \tag{19}$$

The Kalman gains $\mathbf{K}_1$ and $\mathbf{K}_2$ for this LTI system can be obtained resorting to function *kalman* from *MATLAB* resulting in the observer

$$\begin{bmatrix}\hat{\boldsymbol{q}}_{k+1}\\ \hat{\boldsymbol{b}}_{k+1}\end{bmatrix} = \begin{bmatrix}\mathbf{I} & -\frac{\Delta t}{2}\mathbf{I}\\ \mathbf{0} & \mathbf{I}\end{bmatrix}\begin{bmatrix}\hat{\boldsymbol{q}}_k\\ \hat{\boldsymbol{b}}_k\end{bmatrix} + \begin{bmatrix}\frac{\Delta t}{2}\mathbf{I}\\ \mathbf{0}\end{bmatrix}\mathbf{w}_{rk} + \begin{bmatrix}\mathbf{K}_1 & \mathbf{0}\\ \mathbf{0} & \mathbf{K}_2\end{bmatrix}(\mathbf{q}_k - \hat{\mathbf{q}}_k). \tag{20}$$

5. Air-Bearing-Based Attitude Simulator

The test bench provides an inexpensive platform for ground-based testing while imitating the torque-free conditions of a satellite in space. This simulator is composed of 2 main parts: a rotor and a stator. The stator is composed of a small chamber and a plate with a hole. The rotor is a hollow sphere made of plastic that sits on top of the rotor. An air compressor is connected to the small chamber, forcing air through the hole of the plate. This keeps the rotor suspended on a cushion of air and allows the simulator to rotate 360º in roll, pitch and yaw. The main advantage of this setup is the low friction between the plate and the sphere.

Let's consider the gap coordinates (x,y, ϕ) parallel and perpendicular to the curved surface and related to the spherical coordinates (r, θ, ϕ) as $x = R\theta$, $y = R + h - r$, where h is the width of the gap between the rotor and the stator, as depicted in Fig. 1.

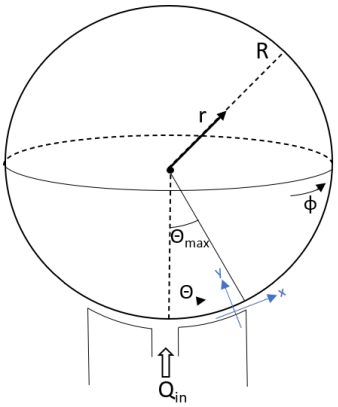

Figure 1: Sphere coordinates (r, θ, ϕ) and auxiliary gap coordinates (x, y, ϕ).

The levitation force is provided by the gauge pressure $P(\theta) - P_{Atm}$ inside the fuid layer:

$$F_{up} = \int\int [P(\theta) - P_{Atm}]\cos(\theta) dA, \tag{21}$$

where dA represents the submerged surface. The pressure field follows from the mass and momentum balance within the fluid. Neglecting the compressibility of the fluid and noting that in steady state the fluid rapidly orients itself on the θ-direction, $\mathbf{u} = u_\theta(r,\theta)\mathbf{e}_\theta$, the mass balance in steady state is

$$\frac{\partial u_\theta}{\partial \theta} sin(\theta) + v_\theta cos(\theta) = 0. \quad (22)$$

5.1. Creeping Flow Approximation

The momentum balance is expressed by the Navier-Stokes equation. For constant density ρ and viscosity μ and neglecting the gravitational effect and the term $\rho(\mathbf{u}.\nabla\mathbf{u})$, it reduces to the known "creeping flow". The velocity profile can be reduced to the well-known planar *Poiseuille* velocity profile for (irrotational) flow between parallel plates:

$$u_\theta(y,\theta) = \frac{1}{2}\frac{6Q}{\pi R h^3 sin(\theta)} y(h-y). \quad (23)$$

where Q is the total flux per unit of time, R is the rotor radius and h is fluid film thickness.

The gauge pressure can be computed by

$$P(\theta) - P_{atm} = \frac{6\mu Q}{\pi h^3} ln\left[\frac{(1-cos(\theta_{max}))sin(\theta)}{(1-cos(\theta))sin(\theta_{max})}\right]. \quad (24)$$

By replacing equation 24 in 21, the levitation force is obtained:

$$F_{up} = \frac{6\mu Q R^2}{h^3}(1-cos(\theta_{max})). \quad (25)$$

Now, by equating the levitation force to the weight of the rotor, $F_g = m_r.g$, the thickness of the fluid layer is obtained:

$$h = \left(\frac{6\mu Q R^2}{m_r g}\right)^{1/3} \left(1-cos(\theta_{max})\right)^{1/3}. \quad (26)$$

The values for the developed test bench are: $\mu = 1.81 \times 10^{-5} Kg/(m.s)$, $R = 0.1m$, $g = 9.81 m/s^2$, $m_r = 1.33Kg$, $Q = 0.00023 m^3/s$, $\theta_{max} = 0.6rad$, $\rho = 1.225 Kg/m^3$, orifice radius of 1mm. These values can be used to compute the thickness of the fluid layer, obtaining $h = 0.15mm$.

5.2. Damping of Rotations

The only source of drag is the viscous drag that causes the angular speed to slow down exponentially as $w(t) = w(0)e^{-t/t_{rel}}$, where t_{rel} is the relaxation time. The relaxation time can be approximately found by:

$$t_{rel} \sim \frac{\rho_{rotor} R h}{\mu}. \quad (27)$$

Replacing the values for the developed test bench, one obtains $t_{rel} = 4.4$ minutes.

6. Prototype

Most of the components of the satellite functional prototype are Commercial Off-The Shelf (COTS), except for the outer structure and the supports, which were 3D printed. A *Raspberry Pi* is connected to an LSM9DS1 IMU, 3 hall-effect sensors and 2 DRV8835 motor drivers. As actuators, the satellite will be provided with 3 momentum wheels aligned with the 3 body axis.

To characterize the IMU noise, data corresponding to 1.5 hours was collected. Its biases are $[-0.11475, 0.10982, -0.044702] o/s$ and $[0.1096, -0.11303, -0.20123] m/s^2$. Its variances are $[0.0029346; 0.0052722; 0.0013492](o/s)^2$, $[7.1815e-05, 0.0001305, 0.0001102](m/s^2)^2$ and $[0.15055, 0.15971, 0.37153](\mu T)^2$. The magnetometer is corrected for soft and hard iron.

Regarding the testbed, the rotor was bought off-the-shelf, the stator was manufactured in bronze and the supports for the 1U CubeSat were 3D printed. The drawings can be found on [11]. As it is evident in Fig. 2, the rotating parts also include the rotor and the supports. The moment of inertia of the rotating parts is

$$\mathbf{J}_{Total} = \begin{bmatrix} 3.58 & -0.0297 & 0.0298 \\ -0.0297 & 3.54 & 0.0122 \\ 0.0298 & 0.0122 & 3.35 \end{bmatrix} \times 10^{-3} Kg.m^2. \quad (28)$$

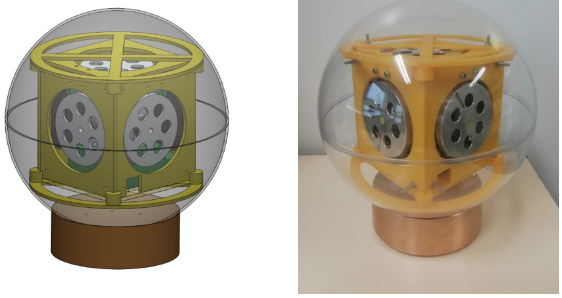

(a) 3D Model (b) Picture

Figure 2: 3D model (Left) and Picture (Right) of the Satellite Prototype Sitting on the Test Bench.

7. Simulation Results

The proposed algorithms for the ADCS system were tested against the realistic environment created within the *MATLAB/Simulink* platform, composed of an orbit propagator, an environment simulator and the spacecraft, sensors and actuators models. The considered orbit is the same as the ISS. The parameters used for the control algorithms are resumed in Tab. 7. The parameters used for the Euler-based complementary filter (F1), quaternion-based complementary filter (F2) and quaternion-based kalman filter (F3) are resumed in Tab. 7.

To test the estimation algorithms, the simulation is initialized with the body and LVLH frames aligned and no angular velocity between these two

frames. No control is applied during one orbit period. The results are depicted on Fig. 3 and 4.

	Parameters
LQR	T = 0.1s; $\mathbf{Q}_L = 0.5.\mathbf{I}_6$; $\mathbf{R}_L$=1e06.$\mathbf{I}_3$
LQRI	T = 0.1s; $\mathbf{Q}_{L_w} = 50\mathbf{I}_3$; $\mathbf{Q}_{L_q} = 0.5\mathbf{I}_3$; $\mathbf{R}_L$=1e06.$\mathbf{I}_3$; $\mathbf{Q}_I$=0.01$\mathbf{I}_3$
Detumbling	$k_{det} = 1.35 \times 10^{-5}$
Mom. Dumping	$k_{md} = -1$

Table 1: Control parameters.

	Parameters
F1	Δt=0.1s; $\mathbf{T}$ = diag([153.6, 256, 153.6]); $\mathbf{R}$ = diag([10, 25, 5]); $\mathbf{Q} = 10^{-3}$. $diag(8000, 8000, 8000, 5, 16, 16, 5, 25, 25)$;
F2	Δt=0.1s; t=0.2;
F3	Δt=0.1s; $\mathbf{R}$ = diag([10,25,5]); $\mathbf{Q}$ = diag([8,8,8,2e-04,2e-04,2e-04]);

Table 2: Filters parameters.

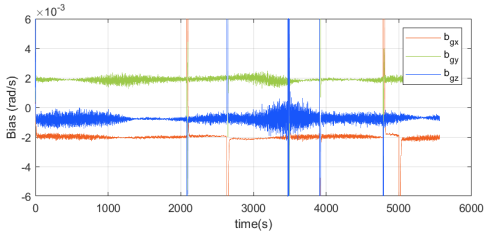

(a) Euler-based Complementary Filter(Zoom).

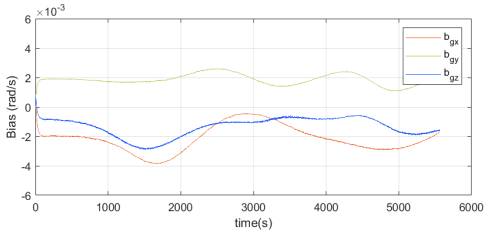

(b) Quaternion-based Kalman filter.

Figure 3: Bias estimation.

To test the nominal mode, the Euler angles are set to 10º and the body rate to zero. The controller is fed with the real state values. The results are shown on Fig. 5, 6, 7, 8, 9 and 10.

The designed controller was applied to the spacecraft described with a Monte Carlo perturbation model: the off diagonal elements of the inertia matrix are randomly selected between 0 and $1 \times 10^{-4} Kg.m^2$; the initial Euler angles between 0º and 90º; the initial angular rates between 0 and 1 º/s. A first order model of the Earth's magnetic field was considered along with the ideal case of $\mathbf{T}_c = -\dot{\mathbf{h}}_w$ and only the magnetic and gravity gradient distur-

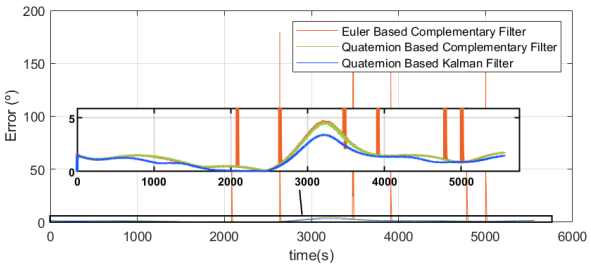

Figure 4: Estimation error.

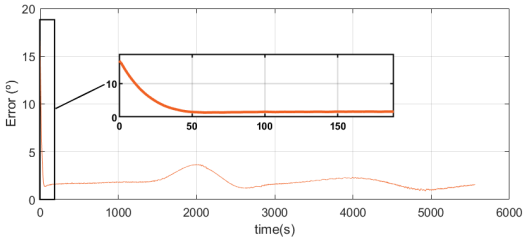

Figure 5: Pointing error for the LQR.

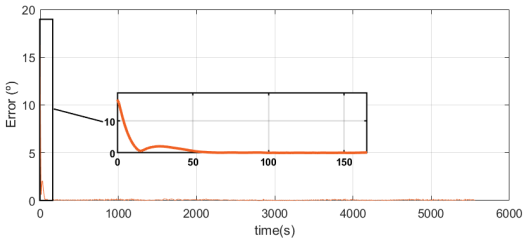

Figure 6: Pointing error for the LQRI.

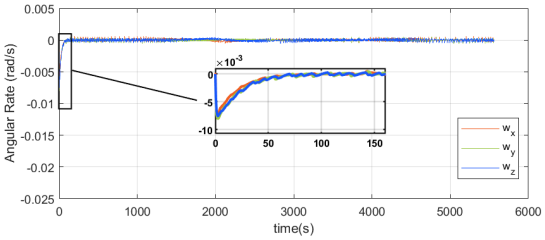

Figure 7: Angular rate for the LQR.

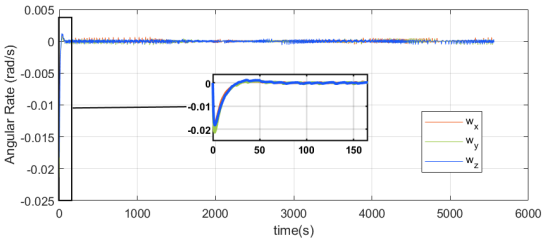

Figure 8: Angular rate for the LQRI.

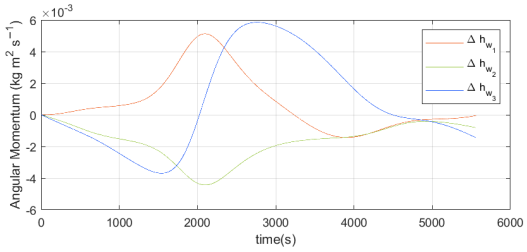

Figure 9: $\Delta \mathbf{h}_w$ for the LQR.

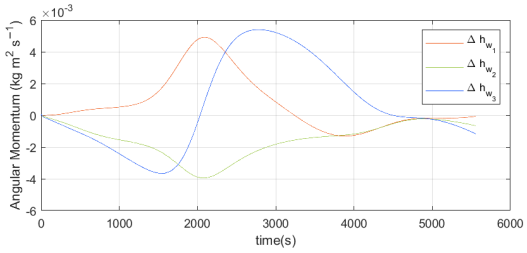

Figure 10: $\Delta \mathbf{h}_w$ for the LQRI.

bances were taken into account. 300 Monte Carlo Simulation runs are conducted (see Fig. 11).

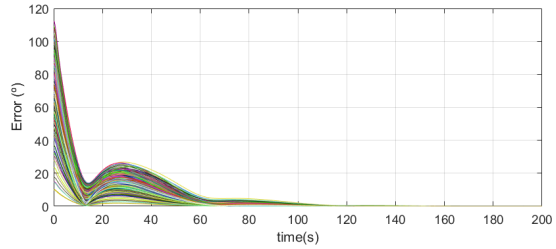

Figure 11: Monte Carlo Simulation for the nominal mode .

Next, detumbling from an initial angular rate of [30, 30, 30] ^{o}/s is tested (Fig. 12 and 13).

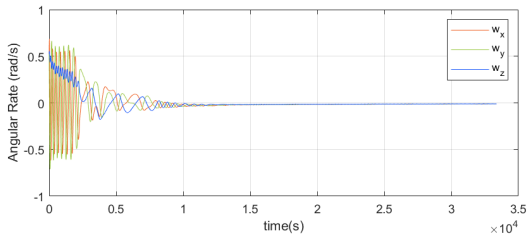

Figure 12: Detumbling with wheels not spinning.

The detumbling is applied to the spacecraft described similarly to the Monte Carlo model from Fig. 11, differing in the initial Euler angles that were selected between 0^{o} and 360^{o} and the initial angular rates between 0 and 30^{o}/s. The wheels are not spinning. The results are plotted in Fig. 14.

Next, the controllers are fed with the estimators.

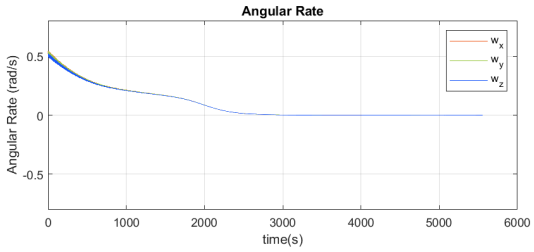

Figure 13: Detumbling with wheels spinning.

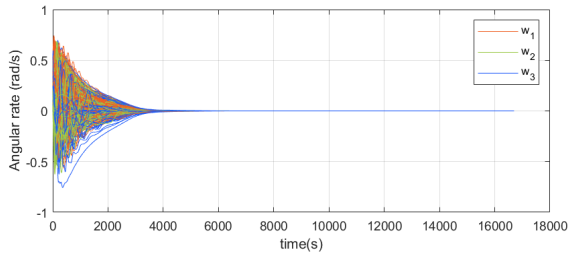

Figure 14: Monte Carlo Simulation for the Detumbling Mode.

This results in 6 simulation cases resumed in Tab. 7. The Euler angles are set to 10^{o} and there is no initial body frame rate.

	LQR	**LQRI**
Euler comp. filter	Case 1	Case 2
Quaternion comp. filter	Case 3	Case 4
Quaternion kalman filter	Case 5	Case 6

Table 3: Simulation cases.

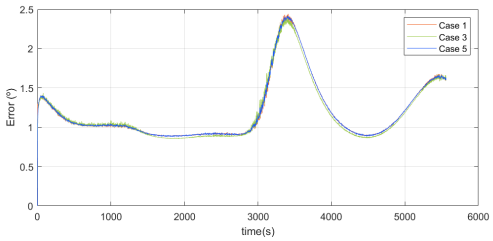

Figure 15: Estimation error for the LQR.

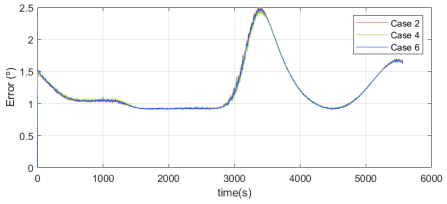

Figure 16: Estimation error for the LQRI.

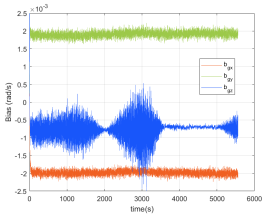

(a) Case 1.

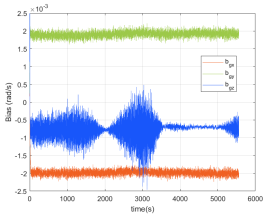

(b) Case 2.

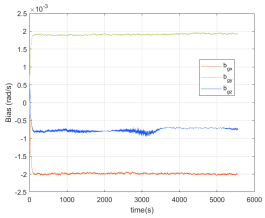

(c) Case 5.

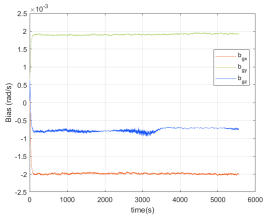

(d) Case 6.

Figure 17: Bias estimation for cases 1, 2, 5 and 6.

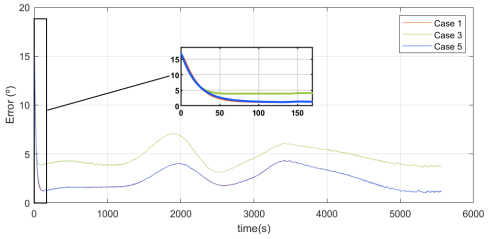

Figure 18: Pointing error for the LQR..

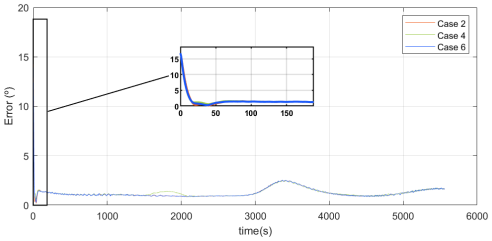

Figure 19: Pointing error for the LQRI.

7.1. Discussion

Regarding the Euler-based complementary filter (see Fig. 4), it is evident that there are peaks in the estimation error. Naturally, these are accompanied by disturbances in the rate gyros bias estimation (see Fig. 3). The estimation is originally done based on the Euler angles formulation. Being the Euler angle domain restricted, each time one of the limits is crossed and there is a discontinuity on the estimation, the filter will deviate from the nominal estimation. However, the nominal performance of this filter is comparable to the quaternion-based complementary filter. Furthermore, the Euler-based complementary filter is able to estimate the gyroscope biases. The quaternion-based kalman filter performance is slightly better than the one from the other filters. The bias estimation, however, is much worse than the one from the Euler-based complementary filter. This is explainable by the fact that the kalman filter was based on a linearization of the kinematics equation around a zero pointing error and body frame rate. When no control is applied, the system deviates significantly from this point. When compared to the other two filters, the SLERP-based filter has the disadvantage of not being able to estimate the gyroscope biases.

Regarding the LQR (see Fig. 5, 7 and 9), it is evident that it is sufficient to stabilize the system. The pointing error, however, is not regulated to zero, even though it remains below 4^{o}. Regarding the adding of the integral action (see Fig. 6, 8 and 10), the pointing error is now regulated to zero. Also, it uses a slightly smaller portion of the range of actuation of the reaction wheels. The Monte Carlo simulation for the nominal mode of the spacecraft (Fig. 11) showed that the controller is robust to different initial conditions.

The results from magnetic detumbling depend whether the momentum wheels are spinning or not, since they provide a resistance to the spacecraft rotation. If the wheels are not rotating, the spacecraft is considered detumbled after three orbits. Otherwise, it takes only one orbit period. In Fig. 14, it is evident that the detumbling is effective for various initial angular rates. Even though stability could only be proven for a diagonal inertia matrix, the results from the Monte Carlo simulation show that the controller is robust to parameter uncertainty in the inertia matrix.

Simulation cases 1, 3 and 5 regard the LQR controller. The pointing accuracy stays bellow 4.5 degrees for cases 1 and 5. For case 3, a pointing accuracy of only roughly 7 degrees was attained (see Fig. 18) due to the fact that the Quaternion-based complementary filter is not able to compensate for the gyroscope bias. Simulation cases 2, 4 and 6 regard the LQR with integrative action controller (Fig. 19). In all 3 cases, the controller is able to align the body frame with the LVLH frame with a pointing accuracy of less than 2.5 degrees. The unavailability of bias estimation in case 4 is compensated, resulting in a similar pointing accuracy.

Regarding the bias estimation (Fig. 17) both the Euler-based complementary filter and the quaternion-based kalman filter are capable of providing an adequate estimation, as opposite to the results without control action. This is due to the fact that the system does not deviate significantly from the linearization point. The estimation error is below 2.5 degrees for all cases (Fig. 15 and 16). The bias estimation is less noisy for cases 5 and 6.

8. Experimental Results

The results from this section regard the control of the developed prototype in 1 direction. With that in mind, the upper part of the rotor sphere was removed and a weight was added at the bottom of the CubeSat, forming a pendulum, so that the pitch and roll errors were compensated by gravity. The inertia on the z axis remains approximately the same and the satellite is not controlled on the x and y body axis.

First, the prototype is set to rotation and the angular velocity decay is measured so as to study the damping of rotations.

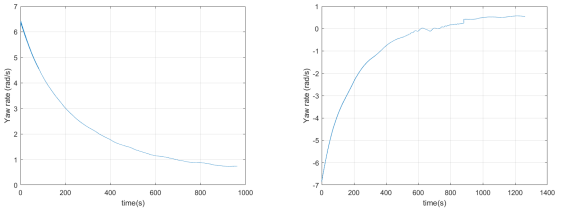

(a) Clockwise rotation decay. (b) Counter-clockwise rotation decay.

Figure 20: Angular velocity decay without actuation when the prototype is set to rotate clockwise (Left) and counter-clockwise (Right).

Next, the 6 cases previously studied are tested in the ground-testing facility, for the yaw-axis only.

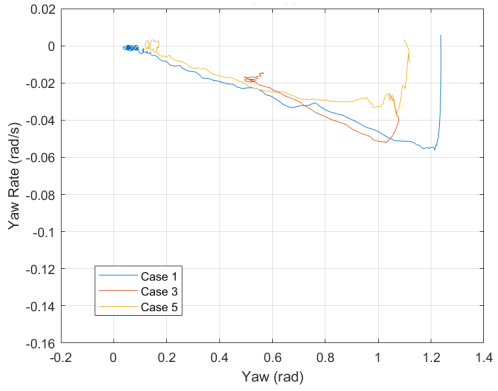

Figure 21: LQR experimental results in the Phase Plane.

8.1. Discussion

As depicted in section 5, the viscous drag causes the angular speed to slow down exponentially. This means that the external torque is proportional to the angular velocity $T_{external} = -k\omega$. Denoting the differential equation of the angular velocity as $\dot{\omega} = -\lambda\omega$, the decay constant, λ, is related to the external torque by the following relation $\lambda = k/I$, where I is the rotating part moment of inertia. Using the function *fit* from the *Curve Fitting Toolbox* of *MATLAB*, the angular velocity decay for the clockwise rotation was best identified by the expression $5.506exp(-0.004196.t) + 0.687$. The counter-clockwise rotation was best identified by $-6.891exp(-0.004301.t) + 0.4926$. This means that the rotations decay more rapidly for counter-clockwise rotations. This goes along with observation, since it was evident that the rotor had a deterministic tendency to rotate clockwise, settling at a given positive yaw rate. So, it is not only the viscous drag that affects the testbed.

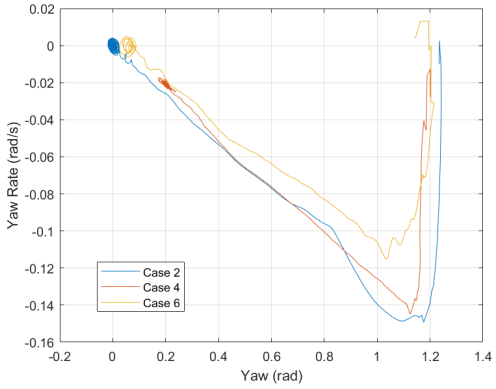

Figure 22: LQR with integral action experimental results in the Phase Plane.

The testbed was required to have disturbance torques at most of the same order of magnitude of those present in space ($10^{-6}N.m$). Approximating the decay constant for the viscous drag by the average of the two previous decay constants: $0.004285s^{-1}$. Note that $\lambda \sim 4 \times 10^{-3}s^{-1}$, $I \sim 3 \times 10^{-3}Kg.m^2$, meaning that $k \sim 1.2 \times 10^{-5}Kg.m^2s^{-1}$. Taking into account that $w \sim 0.1rad/s$, the external torque due to the viscous drag is $T \sim 10^{-6}N.m$, meaning that it is of the same order of magnitude of those present in space.

For the LQR controller (cases 1, 3 and 5), it is evident that the yaw angle is not regulated to zero. The pointing accuracies are 6, 40 and 12 degrees respectively. This lack of accuracy in case 3 was not predicted by the simulations results. In fact, the gyroscope bias used in simulation was identified with the motors turned off. When the motors are turned on, the biases increase significantly. Since this filter is not able to estimate the biases, its use produces the worst results. For the LQR with integrative action, the steady state error is smaller. The pointing accuracies for cases 2, 4 and 6 are 5 degrees, 15 degrees and 6 degrees respectively.

As a final remark on the validity of the obtained results, note that the testbed is affected by an external torque different from the viscous drag. This is evident by the results from Fig. 20. The gravity

torque due to the displacement between the center of mass and the center of rotation could not be completely compensated and contributes to some wobbling of the platform. Other than that, it is inevitable that de viscous drag would deviate the results from the ones on a drag-free environment.

9. Conclusions

Regarding the testbed, theory shows that it is possible to create a full 360^{o} pitch, roll and yaw simulator, even though many other attempts to create such a platform were unsuccessful. The contribution of this work for the effort of creating such a platform is two-folded. Firstly, a review of previous efforts and existent platforms was undertaken. The physics of air-bearing platforms was detailed, after which a platform aiming at full 3 DOF was built. However, only 360^{o} of freedom on the yaw axis was achieved. Further work is required to eliminate the unpredicted aerodynamic torque, the gravity torque due to the displacement between the center of rotation and center of mass, and the disturbance caused by the rib in the junction of the 2 rotor half-spheres.

Regarding the ADCS system, detumbling with magnetic torques is achieved in less than one orbit period if the wheels are spinning at their nominal rate. Regarding the pointing capability, simulation shows that in nominal conditions a pointing accuracy of less than 2.5 degrees is achievable when using the LQR controller with Integral action (LQRI). Coupling with the Quaternion-based Kalman filter showed to be the best choice for cases when the satellite deviates from its nominal position. As a result, coupling of the LQRI controller with the Quaternion-based Kalman filter is suggested for a real application.

Acknowledgements

This work is framed within the context of the NANOSTAR Project [9]. The author would like to thank professor Paulo Oliveira, for the unwearying support and advice.

References

[1] G. F. Avanzini, G. Magnetic detumbling of a rigid spacecraft. *J. Guid. Contr. Dynam.*, 4(35):1326–1334, 2012.

[2] J. Bouwmeester and J. Guo. Survey of worldwide pico- and nanosatellite missions, distributions and subsystem technology. *Acta Astronautica*, 67(7-8):854–862, 2010.

[3] M. W. G. F. Franklin, J. D. Powell. *Digital control of dynamic systems.* Ellis Kagle Press, 3 edition.

[4] C. C. J. Madeiras and P. Oliveira. Vision-aided complementary filter for attitude and position estimation: Design, analysis and experimental validation. *IFAC-PapersOnLine*, 52(12):388–393, 2019. doi:10.1016/j.ifacol.2019.11.274.

[5] C. T. J. Puig-Suari and W. Ahlgren. Development of the standard cubesat deployer and a cubesat class picosatellite. *IEEE Aerospace Conference Proceedings*, page 347–353, 2001, Big Sky, MT, USA,.

[6] F. L. Markley. Spacecraft attitude determination methods. *40th Israel Annual Conference on Aerospace Sciences, Tel Aviv and Haifa, Israel*, 2000.

[7] F. L. Markley and J. L. Crassidis. *Fundamentals of Spacecraft Attitude Determination and Control.* Springer New York Heidelberg Dordrecht London, 2014. ISBN:9781493908011.

[8] D. M. Meissner. A three degrees of freedom test-bed for nanosatellite and cubesat attitude dynamics, determination, and control. Master's thesis, Naval Postgraduate School, Monterey, CA, 2009.

[9] I. S. Programme. Nanostar: Hands-on higher aerospace education through nanosatellite student challenfes. URL https://nanostarproject.eu/, 2020.

[10] J. X. R. Valenti, I. Dryanovski. Keeping a good attitude: A quaternion-based orientation filter for imus and margs. *Sensors*, 8 2015.

[11] B. Ribeiro. Technical drawings of the testbed and satellite prototype. URL: shorturl.at/dgDNZ, 2020.

[12] J. Schwartz, M. Peck, and C. Hall. Historical review of air-bearing spacecraft simulators. *Journal of Guidance, Control, and Dynamics*, 26, 05 2003.

[13] M. Sidi. *Spacecraft Dynamics and Control: A Practical Engineering Approach.* Cambridge University Press, Cambridge, UK, 1997. ISBN:0-521-55072-6.

[14] J. Solà. Quaternion kinematics for the error-state kalman filter. 2015. hal-01122406v5.

[15] K. J. Âstom and R. M. Murray. *Analysis and Design of Feedback Systems.* Princeton University Press, preprint available at http://www.cds.caltech.edu/ murray/am05. edition.

[16] Y. Yang. *Spacecraft modeling, attitude determination, and control : quaternion-based approach.* CRC Press, 2019. ISBN:978-1138331501.